

# Dynamic Modeling and Analysis of Wind Turbine Blade of Piezoelectric Plate Shell

Yinhu Qiao<sup>1,\*</sup>, Chunyan Zhang<sup>1</sup> and Jiang Han<sup>2</sup>

<sup>1</sup>School of Mechanical Engineering College, Anhui Science and Technology University, Fengyang, 233100, China.

<sup>2</sup>School of Mechanical Engineering, Hefei University of Technology, Hefei, 230000, China.

\*Corresponding Author: Yinhu Qiao. Email: qyh7926@163.com.

**Abstract:** This paper presents a theoretical analysis of vibration control technology of wind turbine blades made of piezoelectric intelligent structures. The design of the blade structure, which is made from piezoelectric material, is approximately equivalent to a flat shell structure. The differential equations of piezoelectric shallow shells for vibration control are derived based on piezoelectric laminated shell theory. On this basis, wind turbine blades are simplified as elastic piezoelectric laminated shells. We establish the electro-mechanical coupling system dynamic model of intelligent structures and the dynamic equation of composite piezoelectric flat shell structures by analyzing simulations of active vibration control. Simulation results show that, under wind load, blade vibration is reduced upon applying the control voltage.

**Keywords:** Wind-turbine blade; smart structure; laminated shallow shell; dynamics modeling

## 1 Introduction

Large-scale wind turbines can reduce power generation cost and increase efficiency by exploiting the following relationship between power and swept area  $A$  [1]:

$$P = \frac{1}{2} C_p \rho A V_\infty^3 = \frac{1}{2} C_p \rho \pi R^2 V_\infty^3, \quad (1)$$

where  $C_p$  is the power coefficient,  $R$  is the wind wheel radius,  $\rho$  is the air density,  $A$  is the swept area of a rotor, and  $V_\infty$  is the velocity of wind flow. The air volume and the leaf quality increase with blade length. Long blades also capture more wind energy, but the leaves become vulnerable to dynamic loads and random wind. A lag time exists between the blade vibration control device reaction and the load on the blade, thereby preventing the blade load from being reduced in real time [2-5]. Two types of blade vibration control are possible, namely, passive control and active control. In the early 1990s, active control of blade pitch and yaw was introduced in the United States [6,7]. Synchronous variable pitch of wind turbine blades can be used to vary the pitch torque, avoid stall, and achieve a low wind load on the blade when the wind speed exceeds the rated speed [8]. However, for high wind speed, the blade pitch cannot be adjusted sufficiently fast; thus, wind turbines with synchronous variable pitch are also damaged under a damage load. To deal with this situation, independent variable pitch was introduced, whereby the pitch angle of each blade is controlled independently to alleviate load on the blade. Independent variable pitch control is currently the most advanced load control mechanism for wind turbine blades [7]. With the development of offshore wind power, which dispenses with restrictions such as bridge height for blade transport, wind turbine blades become increasingly large and the load on the blades increases concomitantly. Local control of the aerodynamic load distributed over a blade can be achieved by using a built-in intelligent device [8], which is the concept of the “smart wind wheel.” One technology for unloading force on the blade is active aerodynamic load control [9].

The National Renewable Energy Laboratory at the Technical University of Denmark studied this topic [10,11] by analyzing the potential flow and using a geometry model of cable elasticity and a damping variable airfoil [12] to test the trailing-edge drop airfoil at low and normal force fluctuations. Results show that the vibration direction of the blade can be controlled by the displacement and velocity of the airfoil, and the standard deviation can be reduced to 85%. The standard deviation of the normal force is reduced by detecting the angle of attack. For the FAST (Fatigue, Aerodynamics, Structures, and Turbulence) system, a three-dimensional simulation shows that the harmful load can be reduced by up to 64% [13]. In Holland, the Delft University of Technology Wind Energy Institute studied several smart-wind-wheel control methods [14]. In addition, numerous studies on folding wings (microtabs or microjets) were conducted at the University of California at Davis [15]. Piezoelectric materials with unique properties that allow in situ sensing and control are the leading smart materials [16-18].

## 2 Design and Modeling of Piezoelectric Shell Blade

At present, large wind turbine blades are made of glass fiber-reinforced resin and consist of a skin and a main girder. The piezoelectric materials, as sensing and driving materials, are applied and laid between the upper and lower layers of the glass and steel materials. Along the airfoil, the blade is equivalent to two shallow shell structures, as shown in Fig. 1. The airfoil is composed of a bottom surface for shallow shells, which are designed by using rectangular hyperbolic approximation. The wind turbine blade is approximately equivalent to double curved shallow shells.

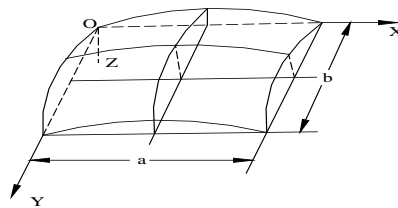


**Figure 1:** Rectangular flat shell [19]

The piezoelectric layer laminated on the shell is a piezoelectric adaptive structure made of a composite matrix layer fixed to a piezoelectric element. In addition to the traditional structural function of bearing, the piezoelectric layer executes the functions of self-perception and self-adjustment by exploiting the electromechanical coupling effect. The differential equation of the piezoelectric laminated shell with a distributed piezoelectric layer is derived from the structural energy function by using first-order shear theory (i.e., The Mindlin-Reissner theory of plates), which considers shear deformation and rotational inertia.

We investigate the dynamic balancing of a composite shell under the action of an external force and pressure power. The goal is for the applied mechanical force (or load) and the control force created by a voltage applied to the piezoelectric shell to offset each other. The piezoelectric force is produced by the converse piezoelectric effect. Fig. 2 shows the piezoelectric shell.

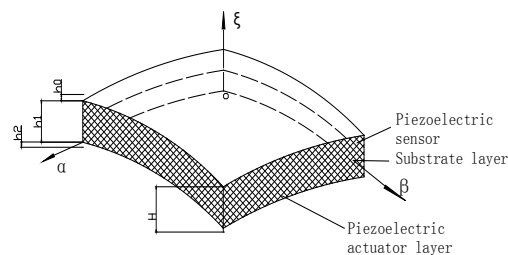


**Figure 2:** Laminated piezoelectric shell [19]

### 3 Finite Element Discrete Model of Piezoelectric Material Shell

#### 3.1 Modeling Curved Shell Unit Geometry

Flat shell theory can be used to establish the surface shell element, which is adopted to solve the difficulty in the selection of displacement mode. The thin shell element of the surface can be obtained by mapping the mother element through the following:

$$x = \sum N_{ix_i,y} = \sum N_{iy_i,z} = \sum N_i z_i \quad (2)$$

The intersection point between the normal and the top surface and the bottom is called the opposite point of the node, and the coordinates of the point of the I node in the entire coordinate system are recorded as

$$x_{i,1} = (x_i \ y_i \ z_i)_{\xi=1}^T, x_{i,-1} = (x_i \ y_i \ z_i)_{\xi=-1}^T \quad (3)$$

The overall coordinate value of the middle surface node i is as follows:

$$x_{i,0} = (x_i \ y_i \ z_i)_{\xi=0}^T = \frac{1}{2}(x_{i,1} + x_{i,-1}) \quad (4)$$

Eq. (4) indicates that the length of the normal line between the top and the bottom of i at the middle point of the middle surface can be obtained, that is, the thickness of the shell at i point, as follows:

$$h_i = [(x_{i,1} - x_{i,-1})^T (x_{i,1} - x_{i,-1})]^{1/2} = [\Delta x_i^T \Delta x_i]^{1/2} \quad (5)$$

In the following form:

$$\Delta x_i = x_{i,1} - x_{i,-1} = (\Delta x_i \ \Delta y_i \ \Delta z_i)^T \quad (6)$$

Thus, the normal vector  $(i_\xi)_i$  of i at the middle plane is

$$(i_\xi)_i = \frac{1}{h_i} [\Delta x_i \ \Delta y_i \ \Delta z_i] \quad (7)$$

This analysis suggests that the overall coordinate value of any point  $(\xi_i, \eta_i, \zeta_i)$  on the normal line at i of the middle plane are

$$i_\zeta^i = (x_i \ y_i \ z_i)^T + \frac{\zeta}{2} (\Delta x_i \ \Delta y_i \ \Delta z_i)^T = x_{i,0} + \frac{\zeta}{2} \Delta x_i \quad (8)$$

The coordinates of any point on the middle surface of the element can be obtained by using the shape function of the plane isoparametric element at the eight points on the normal line at each node, as follows:

$$x = (x_i \ y_i \ z_i)_{\xi}^T = \sum_{i=1}^8 N_i(\xi, \eta) I_3 x_\zeta^i = \sum_{i=1}^8 N_i(\xi, \eta) (x_{i,0} + \frac{\zeta}{2} \Delta x_i) \quad (9)$$

The analysis results show that the shape of the determination unit of the superposition approximation of the infinite "layer" between the upper and lower surfaces of the unit is derived from Eqs. (4), (6), and (9). The upper and lower surface layers could be identified when  $\zeta = \pm 1$ , and the shape of the middle surface when  $\zeta = 0$ . The side of the unit can be made up of the middle surface normal (or the approximate middle surface normal) to describe the element shape of the curved shell element. The discrete model of the shell element is shown in Fig. 3.

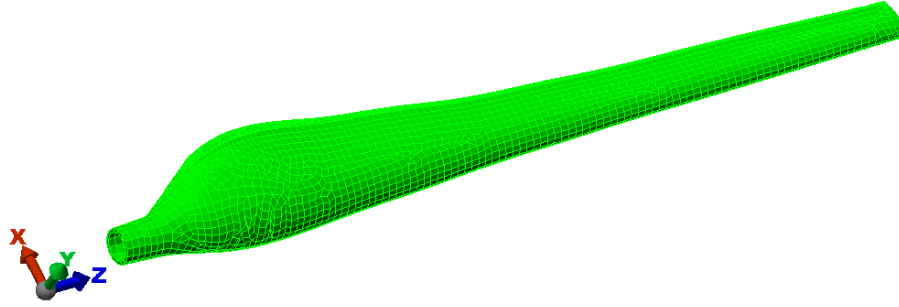


**Figure 3:** Element model of wind turbine blade shell

### 3.2 Modeling Displacement Mode of Curved Shell

For a curved shell, the normal line of the surface varies with the point because the middle surface of the shell is a curved surface. Thus, the two orthogonal axes around the normal line before the deformation vary with the point. Thus, to establish the displacement mode, we must first determine the two orthogonal rotation axes around the one point of the middle plane when the normal deformation takes place.

The unit vectors of the two rotation axes are set at the  $i$  node with  $(\mathbf{i}_\xi)_i$  and  $(\mathbf{i}_\eta)_i$ , but they cannot be uniquely determined only from the normal planes, that is, they should be perpendicular to the  $i$  point. Thus, the following is assumed:

$$(\mathbf{i}_\xi)_i = \frac{\mathbf{i} \times (\mathbf{i}_\zeta)_i}{|\mathbf{i} \times (\mathbf{i}_\zeta)_i|} = -\frac{\Delta z_i}{(\Delta y_i^2 + \Delta z_i^2)^{1/2}} \mathbf{j} + \frac{\Delta y_i}{(\Delta y_i^2 + \Delta z_i^2)^{1/2}} \mathbf{k} \quad (10)$$

If  $(\mathbf{i}_\xi)_i$  is parallel to the  $x$  axis, then the hypothesis should be changed into  $(\mathbf{i}_\xi)_i = \mathbf{j} \times (\mathbf{i}_\zeta)_i / |\mathbf{j} \times (\mathbf{i}_\zeta)_i|$ , whereas the other unit vector of  $(\mathbf{i}_\eta)_i$  is calculated by the following formula:

$$(\mathbf{i}_\eta)_i = (\mathbf{i}_\zeta)_i \times (\mathbf{i}_\xi)_i = \frac{(\Delta y_i^2 + \Delta z_i^2)^{1/2}}{h_i} \mathbf{i} - \frac{\Delta x_i \Delta y_i}{(\Delta y_i^2 + \Delta z_i^2)^{1/2}} \mathbf{j} - \frac{\Delta x_i \Delta z_i}{h_i (\Delta y_i^2 + \Delta z_i^2)^{1/2}} \mathbf{k} \quad (11)$$

If the middle surface normal vector  $(\mathbf{i}_\zeta)_i$  and the rotation angle of the two axes of  $(\mathbf{i}_\xi)_i$  and  $(\mathbf{i}_\eta)_i$  at the node  $i$  are recorded as  $\beta_i$  and  $\alpha_i$ , then the rotation vector can be written as

$$\omega_i = \beta_i (\mathbf{i}_\xi)_i + \alpha_i (\mathbf{i}_\eta)_i \quad (12)$$

If the displacement matrix of node  $i$   $u_i$  or displacement vector  $u_i$  is recorded, then,

$$\mathbf{u}_i = (u_i \ v_i \ w_i)^T, \mathbf{u}_i = u_i \mathbf{i} + v_i \mathbf{j} + w_i \mathbf{k} \quad (13)$$

The displacement of the  $i$  node and  $\zeta$  along the normal line can be composed of the following two parts: the translational part of the node  $i$  and the rotational part caused by the rotation vector, according to which the kinematics can be obtained

$$\begin{aligned} \mathbf{u}_\zeta^i &= \mathbf{u}_i + \mathbf{w}_i \times \frac{\zeta h_i}{2} (\mathbf{i}_\zeta)_i = \mathbf{u}_i + [\beta_i (\mathbf{i}_\xi)_i + \alpha_i (\mathbf{i}_\eta)_i] \times \frac{\zeta h_i}{2} (\mathbf{i}_\zeta)_i \\ &= \mathbf{u}_i + [-\beta_i \frac{\zeta h_i}{2} (\mathbf{i}_\eta)_i + \alpha_i \frac{\zeta h_i}{2} (\mathbf{i}_\xi)_i] = \mathbf{u}_i + \frac{\zeta h_i}{2} ((\mathbf{i}_\xi)_i - (\mathbf{i}_\eta)_i) \begin{pmatrix} \alpha_i \\ \beta_i \end{pmatrix} \end{aligned} \quad (14)$$

or represented as the following matrix form:

$$\mathbf{u}_\zeta^i = \begin{pmatrix} \mathbf{u}_i \\ \mathbf{v}_i \\ \mathbf{w}_i \end{pmatrix} + \frac{\zeta \mathbf{h}_i}{2} \begin{pmatrix} 0 & \mathbf{l}_\eta^i \\ \mathbf{m}_\xi^i & \mathbf{m}_\eta^i \\ \mathbf{n}_\xi^i & \mathbf{n}_\eta^i \end{pmatrix} \begin{pmatrix} \alpha_i \\ \beta_i \end{pmatrix}, \quad (15)$$

$$\text{In where } \mathbf{l}_\eta^i = -\frac{(\Delta y_i^2 + \Delta z_i^2)^{1/2}}{h_i}, \quad \mathbf{m}_\xi^i = -\frac{\Delta z_i}{(\Delta y_i^2 + \Delta z_i^2)^{1/2}}, \quad \mathbf{m}_\eta^i = \frac{\Delta x_i \Delta y_i}{h_i (\Delta y_i^2 + \Delta z_i^2)^{1/2}},$$

$$\mathbf{n}_\xi^i = \frac{\Delta y_i}{h_i (\Delta y_i^2 + \Delta z_i^2)^{1/2}}, \quad \mathbf{n}_\eta^i = \frac{\Delta x_i \Delta z_i}{h_i (\Delta y_i^2 + \Delta z_i^2)^{1/2}} \quad (16)$$

The displacement expression (12) and formula (16) of the i node normal distance node  $\zeta$  (16) are similar to the geometric shape description (9), which can be interpolated by the shape function to the displacement matrix of any point in the unit.

$$\mathbf{u} = (\mathbf{u} \quad \mathbf{v} \quad \mathbf{w})^T = \sum_{i=1}^8 N_i(\xi, \eta) \mathbf{I}_3 \mathbf{u}_\zeta^i$$

$$= \sum_{i=1}^8 N_i(\xi, \eta) \left[ \mathbf{u}_i + \zeta (\phi_\xi^i \quad \phi_\eta^i) \begin{pmatrix} \alpha_i \\ \beta_i \end{pmatrix} \right] \quad (17a)$$

$$\text{where } \phi_\xi^i = \begin{pmatrix} 0 & \frac{h_i}{2} m_\xi^i & \frac{h_i}{2} n_\xi^i \end{pmatrix}, \quad \phi_\eta^i = \frac{h_i}{2} \begin{pmatrix} l_\eta^i & m_\eta^i & n_\eta^i \end{pmatrix} \quad (17b)$$

If the node displacement matrix of unit node i is taken as  $\delta_i = (\mathbf{u}_i \quad \mathbf{v}_i \quad \mathbf{w}_i \quad \alpha_i \quad \beta_i)^T$ , then the unit node displacement matrix is

$$\delta_e = (\delta_1^T \quad \delta_2^T \quad \dots \quad \delta_8^T)^T \quad (18)$$

The element form function matrix is

$$\mathbf{N} = (N_1 \quad N_2 \quad \dots \quad N_8)^T, \quad (19a)$$

where

$$\mathbf{N}_i = (N_i \mathbf{I}_3 \quad \xi N_i \phi_\xi^i \quad \dots \quad \xi N_i \phi_\eta^i)^T \quad (i = 1, 2, \dots, 8) \quad (19b)$$

The displacement modes of such units can be written as follows:

$$\mathbf{u} = \mathbf{N} \delta_e \quad (20)$$

### 3.3 Element Stiffness Matrix of Curved Shell

The analysis results show that the element stiffness matrix  $\mathbf{k}_e$  can be obtained by using the potential energy principle.

$$\mathbf{k}_e = \int_V \mathbf{B}^T \mathbf{D} \mathbf{B} dV = (\mathbf{k}_{ij}^e)_{8 \times 8} \quad (21a)$$

$$\text{where } \mathbf{k}_{ij}^e = \int_V \mathbf{B}_i^T \mathbf{D} \mathbf{B}_j dV = \int_{-1}^1 \int_{-1}^1 \int_{-1}^1 \mathbf{B}_i^T \mathbf{D} \mathbf{B}_j \det \mathbf{J} d\xi d\zeta d\eta \quad (21b)$$

**Table 1:** Properties of composite materials with elasticity. “GFRP” stands for “glass-fiber reinforced resin”

Material	E <sub>1</sub> [GPa]	E <sub>2</sub> [GPa]	G <sub>13</sub> [GPa]	G <sub>23</sub> [GPa]	G <sub>12</sub> [GPa]	ν <sub>12</sub>	ρ [Kg m <sup>-3</sup> ]
GFRP	53.78	17.93	8.96	3.45	8.96	0.25	1900

#### 4 Finite Element Discrete Model of Piezoelectric Material Shell

In the finite element analysis of laminated shells, the following command flow is used to simulate the ANSYS software using the parameters in Tab. 1:

/PREP7 In the ANSYS software.

1) Import the blade model yp.x\_t.

2) Define the type of piezoelectric element and set the piezoelectric parameters:

ET,1,SOLID226,0 !Define the type of solid226 unit

KEYOPT,1,1,1001 !Select the piezo option in the solid226 option

MPTEMP,,,,,,,,

MPTEMP,1,0

DENS,1,7600 !Define the density of piezoceramic

TB,ANEL,1,1,21,0 !Define the stiffness coefficient of piezoelectric ceramics

TBTEMP,0

TBDATA,,1.32e11,7.1e10,7.3e10,,

TBDATA,,1.32e11,7.3e10,,1.15e11

TBDATA,,,,,3.0e10,,

TBDATA,,2.6e10,,2.6e10,,

MPTEMP,,,,,,,, !Define the dielectric constant of piezoelectric ceramics

MPTEMP,1,0

MPDATA,PERX,1,,7.124e-9

MPDATA,PERY,1,,7.124e-9

MPDATA,PERZ,1,,5.841e-9

TB,PIEZ,1,,0 !Define the piezoelectric coefficient of piezoelectric ceramics

TBMODIF,1,1,

TBMODIF,1,2,

TBMODIF,1,3,-4.1

TBMODIF,2,1,

TBMODIF,2,2,

TBMODIF,2,3,-4.1

TBMODIF,3,1,

TBMODIF,3,2,

TBMODIF,3,3,14.1

TBMODIF,4,1,

TBMODIF,4,2,

TBMODIF,4,3,

```
TBMODIF,5,1,
TBMODIF,5,2,10.5
TBMODIF,5,3,
TBMODIF,6,1,10.5
TBMODIF,6,2,
TBMODIF,6,3,
```

3) After the grid is divided, the upper surface node is selected, and the voltage of the coupling node is as follows:

```
CP, 2, volt, all! Add the coupling voltage to the upper surface
*get, n_top, node, 0, num, min! Define the electrode nodes on the upper surface.
```

4) Select again. Select the lower surface node and the coupling voltage, and set the following voltage:

```
CP, 1, volt, all! Add the coupling voltage to the lower surface
*get, n_bot, node, 0, num, min! Define the electrode nodes on the lower surface.
```

```
Nsel, all! Select all nodes
```

```
D, n_bot, volt, 0! Lower surface plus 0 volt voltage
```

```
D, n_top, volt, 400! Top surface plus 400 volt voltage
```

5) Static and modal processing

First, the processing state is selected as a static state, and its static capacitance is obtained in this state. The code and annotations are as follows:

```
/SOL! Enter the processing link
ANTYPE, 0! Choose static processing
/STATUS, SOLU
SOLVE! Solution
*get, CS, node, n_top, RF, CHRG! Obtain the upper electrode value
Fini! End of processing
*SET, CS, ABS (CS) /5! Obtain static capacitance
Modality treatment
/SOLU! Enter the processing link
ANTYPE, 2! Select mode processing
MODOPT, LANB, 20! Define the processing method and the number of substeps
EQSLV, SPAR! Select the processor
MXPAND, 20,, 1! Number of substeps to be displayed
LUMPM, 0
PSTRES, 0
MODOPT, LANB, 20,02000000, OFF! Define the frequency range
D, n_bot, volt, 0! Short on the upper surface
Nsel, all! Select all nodes
/STATUS, SOLU
SOLVE! Solution
/POST1
*SET, nmodes, 20! Define nmodes=20
```

```

*dim, C, array, nmodes! Define an array of capacitors
*dim, L, array, nmodes! Define an array of inductors
*SET, PI2, 2*3.14159! Define PI2=2*3.14159
Set, first! Set the first substep
/com,
*do, I, 7, nmodes! Define a loop from 1 to 20 steps
*get, Fi, mode, I, freq! Obtain the frequency of this step
*get, Qi, node, n_top, RF, CHRG! Obtain the power value of the step
*SET, Omi, Pi2*Fi! Convert line speed to angular velocity
*SET, C (I), (Qi/Omi) **2! Calculate related dynamic capacitance
*SET, L (I), 1/ (Omi**2*C (I))! Calculate related dynamic inductors
/com, Mode%i%! Show the next step in the output window
/com, Resonant frequency F =%Fi% Hz! Display the frequency value in the output window
/com, Dynamic capacitance C =%C (I)% F! Display the dynamic capacitance value in the output window
/com, Dynamic inductance L =%L (I)% H! Display the dynamic inductance value in the output window
/com, charge Q =%Qi% C! Display the power value in the output window
/com,
Set, next! Proceed to the next step
*enddo! The end of the loop
FINISH

```

6) Fig. 4 shows the transient stress (direct integration), an analysis of the parameters of the 200 step, a step of 0.025 s, and gust load curve according to the load on the blade's surface and the model of the wind. The displacement curves under the action of the blade are shown in Fig. 5, and the stress and strain versus time are shown in Fig. 6 and Fig. 7, respectively.

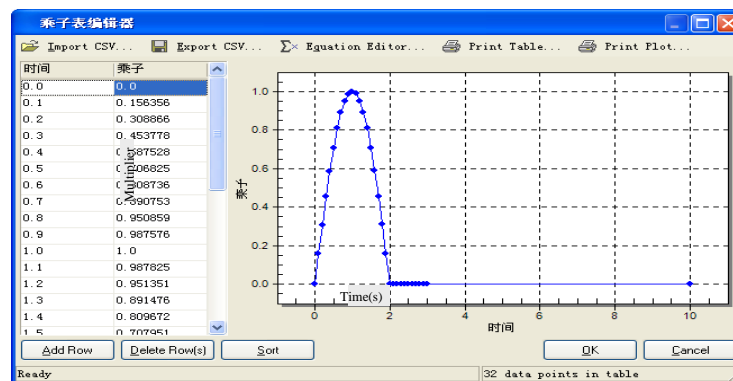
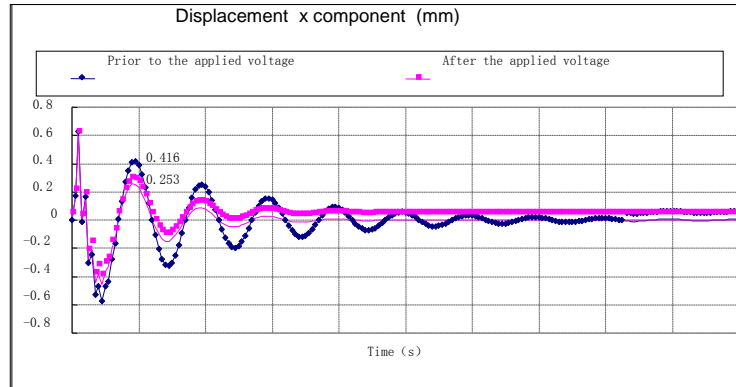
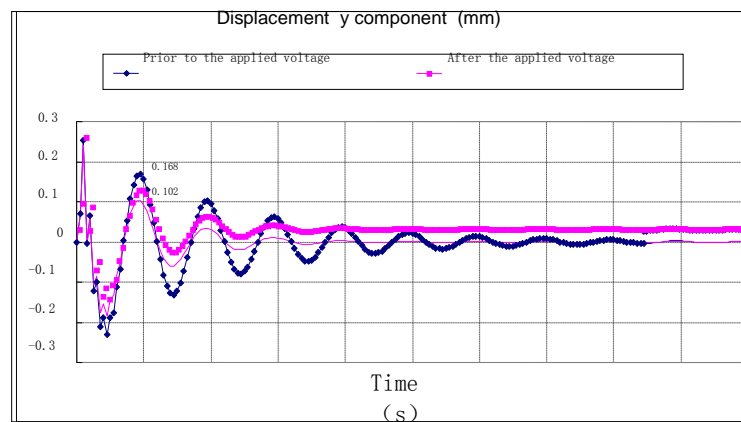


Figure 4: Applied load curve



**Figure 5:** Curve of displacement in the x-axis



**Figure 6:** Curve of displacement in the y-axis

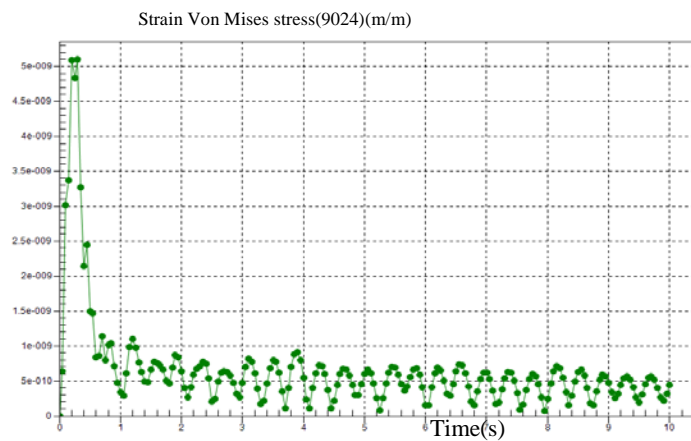


**Figure 7:** Curve of strain in blade root

Results show that before and after the applied potential, the displacement changes are evident. In Fig. 5, x is the displacement components, that is, the control before the maximum vibration amplitude of 0.8 mm, the voltage (400 V) applied to the amplitude is controlled at less than 0.1 mm at last. Fig. 6 shows the same y displacement component of the vibration amplitude before the control at 0.3 mm, after controlling the vibration amplitude within 0.1 mm and rapidly decaying. Fig. 7 shows the strain in blade

root after applying the voltage of 400 V. By contrast, the control voltage is applied to the front with a low external load and slow vibration damping. When a control voltage is applied, the vibration can rapidly decay the vibration amplitude values in the ANSYS command stream, thereby reducing the blade vibration displacement. Thus, the accuracy of the construction of kinetic equations and the engineering value of blade active vibration control using piezoelectric materials is confirmed.

## 5 Conclusion

We discuss the piezoelectric composite blade design for wind turbines and analyze the structural characteristics of piezoelectric laminated shells. We analyze the completely laminated piezoelectric cantilever vibration control and deduce the differential equations for vibration control of piezoelectric laminated shells at the base of wind turbine blades. The system is simplified to a flexible piezoelectric laminated shell to study the use of adaptive inverse control of a piezoelectric ceramic laminated shell structure. Simulation results show the effectiveness of the method.

**Acknowledgement:** The authors thank the following for their support for this work: the Key Project Supported by Foundation University of Science and Technology of Anhui (Nos. JXWD201602 and DTR201501), the Project Supported by Anhui Science and Technology Department (Nos. KJ2018A0536, 1704a0902058, KJ2017ZD44, KJ2015A195, and 1704e1002238), and the Key Construction Discipline Project Supported by University of Science and Technology of Anhui (No. AKZDXK2015C03).

## References

1. Burton, T., Jenkins, N., Sharpe, D., Bossanyi E. (2001). *Wind energy handbook*. West Sussex, England: John Wiley & Sons Ltd.
2. Barlas, T. K., van Kuik, G. A. M. (2010). Review of state of the art in smart rotor control research for wind turbines. *Progress in Aerospace Sciences*, 46(9), 1-27.
3. Bolat, F. C, Sivrioglu. S. (2018). Active control of a small-scale wind turbine blade containing magnetorheological fluid. *Micromachines*, 9(2), 80.
4. Ren, Y. S, Yang, S. L, Du, X. H. (2012). Modeling and Free Vibration Behavior of Rotating Composite Thin-walled Closed-section Beams with SMA Fibers. *Chinese Journal of Mechanical Engineering*, 25(5), 1029-1043.
5. Qiao, Y. H., Han, J., Zhang, C. Y, Chen, J. P. (2012). Modeling smart structure of wind turbine blade. *Applied Composite Materials*, 19(3-4), 491-498.
6. Wingerden, van, Hulskamp, J. W, Barlas, A. T., Houtzager I., Bersee, H. et al. (2011). Two-degree-of-freedom active vibration control of a prototyped "smart" rotor. *IEEE Transactions on Control Systems Technology*, 19(2), 284-296.
7. National Research Council Authoring Organizations (1991): Committee on assessment of research needs for wind turbine rotor materials technology. *Assessment of Research Needs for Wind Turbine Rotor Materials Technology*.
8. Berg, D. E, Wilson, D. G, Resor, B. R., Barlas, T., Kuik, G. V. (2009): Active aerodynamic blade load control impacts on utility-scale wind turbines. *AWEA Wind Power 2009 Conference & Exhibition*.
9. Troldborg, N. (2005). Computational study of the RISO-18 airfoil with a hinged flap providing variable trailing edge geometry. *Wind Engineering*, 29(2), 89-113.
10. Gaunaa, M. (2010). Unsteady two-dimensional potential-flow model for thin variable geometry airfoils. *Wind Energy*, 13(2), 67-192.
11. Houtzager, Wingerden, I., van, J. W., Verhaegen, M. (2013). Rejection of periodic wind disturbances on a smart rotor test section using lifted repetitive control. *IEEE Transactions on Control Systems Technology*, 21(2), 347-359.
12. Buhl, T., Gaunaa, M., Bak, C. (2005): Potential load reduction using airfoils with variable trailing edge geometry. *Solar Energy Engineering*, 127(4), 503-516.

13. Andersen, P. B., Gaunaa, M., Bak, C., Buhl, T. (2006): Load alleviation on wind turbine blades using variable airfoil geometry. *European Wind Energy Conference and Exhibition*.
14. Qiao, Y. H., Han, J., Zhang, C. Y., Chen J. P., Yi, K. C. (2012). Finite element analysis and vibration suppression control of smart wind turbine blade. *Applied Composite Materials*, 19(3-4), 747-754.
15. Baker, J. P., Standish, K. J., van Dam, C. P. (2007). Two-dimensional wind tunnel and computational investigation of a microtab modified airfoil. *Journal of Aircraft*, 44(2), 563-572.
16. Blaylock, M. L. (2012). *Computational investigation on the application of using microjets as active aerodynamic load control for wind turbines (Ph.D. Thesis)*. Dissertations & Theses-Gradworks.
17. Olmi, C., Song, G. B., Shieh, L. S. et al. (2011): A low cost miniature PZT amplifier for wireless active structural health monitoring. *Smart Structures and Systems*, 5(5), 365-378.
18. Yue, H. H. (2009). Research on an active control of precision smart flexible paraboloidal shell systems (*Ph.D. Thesis*). Harbin Institute of Technology, Harbin.
19. Qiao, Y. H., Han, J., Zhang, C. Y., Chen, J. (2016): Dynamical modeling and analysis of wind turbine blade with piezoelectric plate shell. *Acta Energiæ Solaris Sinica*, 37(6), 1560-1565.